Journal of Computational Physics 404 (2020) 109105

Contents lists available at ScienceDirect

Journal of Computational Physics

www.elsevier.com/locate/jcp

High-order Runge-Kutta discontinuous Galerkin methods with a new type of multi-resolution WENO limiters

Jun Zhu [a,1], Jianxian Qiu [b,*,2], Chi-Wang Shu [c,3]

[a] College of Science, Nanjing University of Aeronautics and Astronautics, Nanjing, Jiangsu 210016, PR China
[b] School of Mathematical Sciences and Fujian Provincial Key Laboratory of Mathematical Modeling and High-Performance Scientific Computing, Xiamen University, Xiamen, Fujian 361005, PR China
[c] Division of Applied Mathematics, Brown University, Providence, RI 02912, USA

ARTICLE INFO

Article history:
Received 27 June 2019
Received in revised form 31 October 2019
Accepted 5 November 2019
Available online 13 November 2019

Keywords:
Runge-Kutta discontinuous Galerkin method
Multi-resolution WENO limiter
Accuracy
Non-oscillatory solution

ABSTRACT

In this paper, a new type of multi-resolution weighted essentially non-oscillatory (WENO) limiters for high-order Runge-Kutta discontinuous Galerkin (RKDG) methods is designed. This type of multi-resolution WENO limiters is an extension of the multi-resolution WENO finite volume and finite difference schemes developed in [43]. Such new limiters use information of the DG solution essentially only within the troubled cell itself, to build a sequence of hierarchical L^2 projection polynomials from zeroth degree to the highest degree of the RKDG method. The second-order, third-order, fourth-order, and fifth-order RKDG methods with these multi-resolution WENO limiters have been developed as examples, which could maintain the original order of accuracy in smooth regions and could simultaneously suppress spurious oscillations near strong discontinuities. The linear weights of such new multi-resolution WENO limiters can be any positive numbers on the condition that their sum equals one. This is the first time that a series of polynomials of different degrees within the troubled cell itself are applied in a WENO fashion to modify the DG solutions in the troubled cell. These new WENO limiters are very simple to construct, and can be easily implemented to arbitrary high-order accuracy and in higher dimensions. Such spatial reconstruction methodology improves the robustness in the numerical simulation on the same compact spatial stencil of the original DG methods. Benchmark examples are given to demonstrate the good performance of these RKDG methods with the associated multi-resolution WENO limiters.

1. Introduction

In this paper, we adapt the new type of multi-resolution weighted essentially non-oscillatory (WENO) finite volume methodology [43] as limiters for high-order Runge-Kutta discontinuous Galerkin (RKDG) finite element methods [6–10], for solving one-dimensional nonlinear hyperbolic conservation laws

* Corresponding author.
E-mail addresses: zhujun@nuaa.edu.cn (J. Zhu), jxqiu@xmu.edu.cn (J. Qiu), chi-wang_shu@brown.edu (C.-W. Shu).

[1] Research was supported by Science Challenge Project, No. TZ2016002 and NSFC grant 11872210.
[2] Research was supported by NSFC grant 11571290, NSAF Joint Fund grant U1630247 and Science Challenge Project, No. TZ2016002.
[3] Research was supported by NSF grant DMS-1719410.

https://doi.org/10.1016/j.jcp.2019.109105
0021-9991/

$$\begin{cases} u_t + f(u)_x = 0, \\ u(x,0) = u_0(x), \end{cases} \tag{1.1}$$

and two-dimensional nonlinear hyperbolic conservation laws

$$\begin{cases} u_t + f(u)_x + g(u)_y = 0, \\ u(x,y,0) = u_0(x,y). \end{cases} \tag{1.2}$$

The main objective of the paper is to obtain a simple and robust high-order spatial limiting procedure to simultaneously keep uniform high-order accuracy in smooth regions and sustain sharp, non-oscillatory shock transitions in non-smooth regions for arbitrary high-order RKDG methods on structured meshes.

Let us first review briefly the history of DG methods. In 1973, Reed and Hill [31] proposed the first discontinuous Galerkin (DG) method in the framework of neutron transport. Then a major development of the DG method was carried out by Cockburn et al. in a series of papers [6–10], in which they established a framework to solve nonlinear time dependent hyperbolic conservation laws by using explicit, nonlinearly stable high-order Runge-Kutta time discretizations [35] and DG discretization in space with exact or approximate Riemann solvers as interface fluxes and total variation bounded (TVB) limiter [33] to achieve essentially non-oscillatory property for strong discontinuities. From then on, such schemes are termed as RKDG methods. But it is not easy to solve (1.1) and (1.2) well, because solutions might contain strong discontinuities even if the initial conditions are smooth enough. Discontinuous Galerkin (DG) methods can capture weak discontinuities without further modification. However, for problems with strong discontinuities, the numerical solution might have significant spurious oscillations near strong shocks or contact discontinuities, especially for high-order numerical methods. A common strategy to control these spurious oscillations is to apply a nonlinear limiter. One type of limiters is based on slope modification, such as the *minmod* type limiters [6–8,10], the moment based limiter [1], and an improved moment limiter [3], etc. These limiters can control the spurious oscillations well, however they may degrade numerical accuracy when mistakenly applied in smooth regions. Another type of limiters is based on the weighted essentially non-oscillatory (WENO) methodology [11,18,19,25,32], which can achieve high-order accuracy in smooth regions and keep essentially non-oscillatory property near strong discontinuities. The WENO limiters [26,28,29,42] and Hermite WENO limiters [27,30] belong to the second type of limiters. These limiters are designed in a finite volume WENO fashion, but they need a wider spatial stencil for obtaining high-order schemes. Therefore, it is difficult to implement them for multi-dimensional problems, especially on unstructured meshes, such as triangular meshes or tetrahedral meshes.

Recently, a new type of simple and compact multi-resolution finite difference/volume WENO schemes is designed in [43] for solving hyperbolic conservation laws on structured meshes, in which only the information defined on a hierarchy of nested central spatial stencils is used and no equivalent multi-resolution representation [13–17] is introduced. These new WENO schemes use the same large stencils as that of the classical WENO schemes in [19,34], could obtain the optimal order of accuracy in smooth regions, and could gradually degrade to first order so as to suppress spurious oscillations near strong discontinuities. The linear weights of these multi-resolution WENO schemes can be any positive numbers on the condition that their sum is one. These new multi-resolution WENO schemes are simple to construct and can be easily implemented to arbitrary high-order accuracy and in higher dimensions. In this paper, we will adapt and apply such new multi-resolution WENO schemes as limiters for high-order RKDG methods. Two major advantages of these multi-resolution WENO limiters are the compactness of their spatial stencil, which essentially only contain the troubled cell itself with information from neighboring cells used only to determine the smoothness indicator of the zeroth degree polynomial in the hierarchy, and the simplicity in implementation, especially for unstructured meshes [44] (which will however not be discussed in this paper, we use structured meshes in this paper to demonstrate the main idea of our new limiter). In order to keep the advantages of the compact stencil and simplicity of linear weights, we make a small modification of the procedure in [43], using orthogonal basis and L^2 projection to define the sequence of hierarchical polynomials of different degrees in the troubled cell. This modification facilitates the achievement of strict conservation and the maintanance of as much information of the original polynomial in the troubled cell as possible through the mechanism of a gradual degradation to lower degree polynomials in a L^2 projection fashion with the spatial WENO procedure. Numerical experiments indicate the good behavior of the resulting scheme in its robustness and sharp shock transition.

This paper is organized as follows. In section 2, we give a brief review of the RKDG methods for one-dimensional and two-dimensional cases. In section 3, we give the details of the new two-dimensional multi-resolution WENO limiters for scalar and system cases, and omit the similar narration of one-dimensional multi-resolution WENO limiters for simplicity. Then we demonstrate the good performance of these high-order RKDG methods with multi-resolution WENO limiters for one-dimensional and two-dimensional time dependent examples in section 4. Finally, concluding remarks are given in section 5.

2. A brief review of the RKDG method

In this section, we give a brief review of the RKDG methods for solving hyperbolic conservation laws. For the one-dimensional case, given a partition of the computational domain consisting of cells $I_j = [x_{j-\frac{1}{2}}, x_{j+\frac{1}{2}}]$, $j = 1, \cdots, N$, we denote the cell center by $x_j = \frac{1}{2}(x_{j-\frac{1}{2}} + x_{j+\frac{1}{2}})$, and the cell size by $\Delta x_j = x_{j+\frac{1}{2}} - x_{j-\frac{1}{2}}$. The DG method gets its solution

as well as its test function from the space $V_h^k = \{v(x) : v(x)|_{I_j} \in \mathbb{P}^k(I_j)\}$, where $\mathbb{P}^k(I_j)$ denotes the set of polynomials of degree at most k defined on I_j. We adopt a local orthonormal basis over I_j, $\{v_l^{(j)}(x),\ l = 0, 1, ..., k\}$:

$$\begin{aligned} v_0^{(j)}(x) &= 1, \\ v_1^{(j)}(x) &= \sqrt{12}(\tfrac{x-x_j}{\Delta x_j}), \\ v_2^{(j)}(x) &= \sqrt{180}\left((\tfrac{x-x_j}{\Delta x_j})^2 - \tfrac{1}{12}\right), \\ v_3^{(j)}(x) &= \sqrt{2800}\left((\tfrac{x-x_j}{\Delta x_j})^3 - \tfrac{15}{100}(\tfrac{x-x_j}{\Delta x_j})\right), \\ v_4^{(j)}(x) &= \sqrt{44100}\left((\tfrac{x-x_j}{\Delta x_j})^4 - \tfrac{3}{14}(\tfrac{x-x_j}{\Delta x_j})^2 + \tfrac{3}{560}\right), \\ &..... \end{aligned} \tag{2.3}$$

The one-dimensional solution $u_h(x,t) \in V_h^k$ can be written as:

$$u_h(x,t) = \sum_{l=0}^{k} u_j^{(l)}(t) v_l^{(j)}(x), \quad x \in I_j, \tag{2.4}$$

and the degrees of freedom $u_j^{(l)}(t)$ are the moments defined by

$$u_j^{(l)}(t) = \frac{1}{\Delta x_j} \int_{I_j} u_h(x,t) v_l^{(j)}(x) dx, \quad l = 0, ..., k. \tag{2.5}$$

In order to obtain the approximation solution, we evolve the degrees of freedom $u_j^{(l)}(t)$:

$$\begin{aligned} &\tfrac{d}{dt} u_j^{(l)}(t) = \tfrac{1}{\Delta x_j}\left(\textstyle\int_{I_j} f(u_h(x,t)) \tfrac{d}{dx} v_l^{(j)}(x) dx - \hat{f}(u^-_{j+\frac{1}{2}}, u^+_{j+\frac{1}{2}}) v_l^{(j)}(x_{j+\frac{1}{2}}) \quad + \hat{f}(u^-_{j-\frac{1}{2}}, u^+_{j-\frac{1}{2}}) v_l^{(j)}(x_{j-\frac{1}{2}})\right), \\ &\quad l = 0, ..., k, \end{aligned} \tag{2.6}$$

where $u^{\pm}_{j+\frac{1}{2}} = u_h(x^{\pm}_{j+\frac{1}{2}}, t)$ are the left and right limits of the discontinuous solution $u_h(x,t)$ at the interface $x_{j+\frac{1}{2}}$, and $\hat{f}(u^-_{j+\frac{1}{2}}, u^+_{j+\frac{1}{2}})$ is a monotone flux for the scalar case and an approximate Riemann solver for the system case. For the two-dimensional case, given a partition of the computational domain with rectangular meshes consisting of the cells $I_{ij} = I_i \times J_j = [x_{i-\frac{1}{2}}, x_{i+\frac{1}{2}}] \times [y_{j-\frac{1}{2}}, y_{j+\frac{1}{2}}]$, $i = 1, \cdots, N_x$ and $j = 1, \cdots, N_y$ with the cell sizes $x_{i+\frac{1}{2}} - x_{i-\frac{1}{2}} = \Delta x_i$, $y_{j+\frac{1}{2}} - y_{j-\frac{1}{2}} = \Delta y_j$, and cell centers $(x_i, y_j) = (\frac{1}{2}(x_{i+\frac{1}{2}} + x_{i-\frac{1}{2}}), \frac{1}{2}(y_{j+\frac{1}{2}} + y_{j-\frac{1}{2}}))$, the function space is defined by $W_h^k = \{v(x,y) : v(x,y)|_{I_{i,j}} \in \mathbb{P}^k(I_{i,j})\}$ as the piecewise polynomial space of degree at most k defined on $I_{i,j}$. We also adopt a local orthonormal basis over $I_{i,j}$, $\{v_l^{(i,j)}(x,y),\ l = 0, 1, ..., K;\ K = \frac{(k+1)(k+2)}{2} - 1\}$:

$$\begin{aligned} v_0^{(i,j)}(x,y) &= 1, \\ v_1^{(i,j)}(x,y) &= v_1^{(i)}(x), \\ v_2^{(i,j)}(x,y) &= v_1^{(j)}(y), \\ v_3^{(i,j)}(x,y) &= v_2^{(i)}(x), \\ v_4^{(i,j)}(x,y) &= v_1^{(i)}(x) v_1^{(j)}(y), \\ v_5^{(i,j)}(x,y) &= v_2^{(j)}(y), \\ v_6^{(i,j)}(x,y) &= v_3^{(i)}(x), \\ v_7^{(i,j)}(x,y) &= v_2^{(i)}(x) v_1^{(j)}(y), \\ v_8^{(i,j)}(x,y) &= v_1^{(i)}(x) v_2^{(j)}(y), \\ v_9^{(i,j)}(x,y) &= v_3^{(j)}(y), \\ v_{10}^{(i,j)}(x,y) &= v_4^{(i)}(x), \\ v_{11}^{(i,j)}(x,y) &= v_3^{(i)}(x) v_1^{(j)}(y), \\ v_{12}^{(i,j)}(x,y) &= v_2^{(i)}(x) v_2^{(j)}(y), \end{aligned} \tag{2.7}$$

$$
\begin{aligned}
v_{13}^{(i,j)}(x,y) &= v_1^{(i)}(x)v_3^{(j)}(y),\\
v_{14}^{(i,j)}(x,y) &= v_4^{(j)}(y),\\
&\cdots\cdots
\end{aligned}
$$

The two-dimensional solution $u_h(x,y,t) \in W_h^k$ can be written as:

$$
u_h(x,y,t) = \sum_{l=0}^{K} u_{i,j}^{(l)}(t) v_l^{(i,j)}(x,y), \quad (x,y) \in I_{i,j}, \tag{2.8}
$$

and the degrees of freedom $u_{i,j}^{(l)}(t)$ are the moments defined by

$$
u_{i,j}^{(l)}(t) = \frac{1}{\Delta x_i \Delta y_j} \int_{I_{i,j}} u_h(x,y,t) v_l^{(i,j)}(x,y)dxdy, \quad l = 0, ..., K. \tag{2.9}
$$

In order to determine the approximation solution, we evolve the degrees of freedom $u_{i,j}^{(l)}(t)$:

$$
\begin{aligned}
&\tfrac{d}{dt}u_{i,j}^{(l)}(t) = \tfrac{1}{\Delta x_i \Delta y_j}\Big(\int_{I_{i,j}}\Big(f(u_h(x,y,t))\tfrac{\partial}{\partial x}v_l^{(i,j)}(x,y) + g(u_h(x,y,t))\tfrac{\partial}{\partial y}v_l^{(i,j)}(x,y)\Big)dxdy\\
&- \int_{I_j}\Big(f(u_h(x_{i+\frac12},y,t))v_l^{(i,j)}(x_{i+\frac12},y) - f(u_h(x_{i-\frac12},y,t))v_l^{(i,j)}(x_{i-\frac12},y)\Big)dy\\
&- \int_{I_i}\Big(g(u_h(x,y_{j+\frac12},t))v_l^{(i,j)}(x,y_{j+\frac12}) - g(u_h(x,y_{j-\frac12},t))v_l^{(i,j)}(x,y_{j-\frac12})\Big)dx\Big),\\
&l = 0, ..., K.
\end{aligned} \tag{2.10}
$$

In (2.10), the integrals are computed by suitable numerical quadratures. Notice that the flux functions f and g along the cell interfaces are replaced by monotone numerical fluxes (or approximate Riemann solvers in the system case) to ensure stability.

Then the semi-discrete schemes (2.6) and (2.10) can be discretized in time by a third-order TVD Runge-Kutta time discretization method [35]:

$$
\begin{cases}
u^{(1)} &= u^n + \Delta t L(u^n),\\
u^{(2)} &= \frac34 u^n + \frac14 u^{(1)} + \frac14 \Delta t L(u^{(1)}),\\
u^{n+1} &= \frac13 u^n + \frac23 u^{(2)} + \frac23 \Delta t L(u^{(2)}),
\end{cases} \tag{2.11}
$$

to obtain a fully discrete scheme both in space and in time.

To explain how to apply a nonlinear limiter for the RKDG methods as shown in [39], we adopt a forward Euler time discretization of (2.6) and (2.10) as examples. For the one-dimensional case, starting from a solution $u_h^n \in V_h^k$ at time level n (u_h^0 is taken as the L^2 projection of the given initial condition into V_h^k), we limit it to obtain a new function $u^{n,new}$ before advancing it to the next time level. We need to find $u_h^{n+1} \in V_h^k$ which satisfies

$$
\int_{I_j} \frac{u_h^{n+1} - u_h^{n,new}}{\Delta t} v\,dx - \int_{I_j} f(u_h^{n,new}) v_x\,dx + \hat{f}_{j+\frac12}^{n,new} v(x_{j+\frac12}^-) - \hat{f}_{j-\frac12}^{n,new} v(x_{j-\frac12}^+) = 0, \tag{2.12}
$$

for all test functions $v(x) \in V_h^k$. For the two-dimensional case, starting from a solution $u_h^n \in W_h^k$ at time level n, we limit it to obtain a new function $u^{n,new}$ before advancing it to the next time level. We need to find $u_h^{n+1} \in W_h^k$ which satisfies

$$
\begin{aligned}
&\int_{I_{i,j}} \tfrac{u_h^{n+1} - u_h^{n,new}}{\Delta t} v\,dxdy - \int_{I_{i,j}} \big(f(u_h^{n,new})v_x + g(u_h^{n,new})v_y\big)dxdy\\
&+ \int_{I_j}\Big(\hat{f}(u_h^{n,new}|_{x=x_{i+\frac12}})v(x_{i+\frac12}^-,y) - \hat{f}(u_h^{n,new}|_{x=x_{i-\frac12}})v(x_{i-\frac12}^+,y)\Big)dy\\
&+ \int_{I_i}\Big(\hat{g}(u_h^{n,new}|_{y=y_{j+\frac12}})v(x,y_{j+\frac12}^-) - \hat{g}(u_h^{n,new}|_{y=y_{j-\frac12}})v(x,y_{j-\frac12}^+)\Big)dx = 0,
\end{aligned} \tag{2.13}
$$

for all test functions $v(x,y) \in W_h^k$. Since the one-dimensional limiting procedure of obtaining $u_h^{n,new}|_{I_j}$ is similar to and simpler than the two-dimensional case, we will omit it for simplicity and focus on how to obtain the two-dimensional $u_h^{n,new}|_{I_{i,j}}$ in details. For simplicity, we omit the sup-index n in $u_h^{n,new}|_{I_{i,j}}$, if it does not cause confusion in the following.

3. Multi-resolution WENO limiter in two dimensions

In this section, we describe the details of the new multi-resolution WENO procedure as a limiter for second-order, third-order, fourth-order, and fifth-order RKDG methods in two-dimensional scalar and system cases and omit its one-dimensional case for simplicity.

3.1. Two-dimensional troubled cell indicator

An important component of the limiter is to detect the troubled cells, which are cells that may contain strong discontinuities and in which the multi-resolution WENO limiter is applied. In this paper, we apply a new modified version of the classical KXRCF shock detection technique [20] to detect troubled cells. Other trouble cell detectors can of course also be used, but our emphasis in this paper is not to study the pros and cons of various trouble cell indicators. As shown in [20], we divide the boundary of the target cell $I_{i,j}$ into two parts: $\partial I_{i,j}^{-}$ and $\partial I_{i,j}^{+}$, where the flow is into and out of $I_{i,j}$, respectively. As shown in [12], Fu and Shu noted that the scaling of $\Delta x_j^{\frac{k+1}{2}}$ tends to mark a lot more troubled cells than necessary for high-order DG methods. They decreased the power of Δx_j to be $\frac{\min(k,2)+1}{2}$, which seems to be strong enough to single out discontinuities [12]. In the two-dimensional case, we define the cell $I_{i,j}$ as a troubled cell when

$$\frac{|\int_{\partial I_{i,j}^{-}}(u_h(x,y,t)|_{I_{i,j}}-u_h(x,y,t)|_{I_l})ds|}{h_{i,j}^{R}|\partial I_{i,j}^{-}|\cdot|||\widehat{u_h}(x,y,t)|_{\partial I_{i,j}}|||}\geq C_k, \tag{3.1}$$

where $R=1$ for $k=1$ and $R=1.5$ for $k>1$, $h_{i,j}$ is the radius of the circumscribed circle in cell $I_{i,j}$, and C_k is a constant, usually, we take $C_k=1$ [20]. Here I_l denotes the neighboring cell of $I_{i,j}$ on the side of $\partial I_{i,j}^{-}$. $u_h(x,y,t)$ is the numerical solution corresponding to the indicator variable(s) and $|||\widehat{u_h}(x,y,t)|_{\partial I_{i,j}}|||$ is defined as the minimum value of $|u_h(x,y,t)|$ along $\partial I_{i,j}$. By using (3.1), we do not need to adopt different types of C_k to compute multi-dimensional test problems in [12] and can simply set $C_k=1$ in all numerical computations, unless specified otherwise. This new modified KXRCF shock detection technique is simple and robust enough to catch strong discontinuities without identifying excessive troubled cells inside the computational field.

3.2. Two-dimensional multi-resolution WENO limiting procedure

In this subsection, we first give details of the multi-resolution WENO limiter for two-dimensional scalar case. The idea, similar to the one-dimensional case which is omitted, is to reconstruct a new polynomial on the troubled cell $I_{i,j}$ which is a convex combination of polynomials of different degrees: the DG solution polynomial on this cell and a sequence of hierarchical "modified" solution polynomials based on the L^2 projection methodology. The nonlinear weights in the convex combination coefficients follow the standard WENO procedure [43]. For simplicity, we also rewrite $u_h(x,y,t)$ to be $u_h(x,y)\in W_h^k=\{v(x,y):v(x,y)|_{I_{i,j}}\in\mathbb{P}^k(I_{i,j})\}$ in the following, if it does not cause confusion.

Step 1.1. Define a series of polynomials of different degrees on the troubled cell $I_{i,j}$. We construct polynomials $q_\ell(x,y),\ell=0,\ldots,k$, which satisfy

$$\int_{I_{i,j}} q_\ell(x,y)v_l^{(i,j)}(x,y)dxdy=\int_{I_{i,j}} u_h(x,y)v_l^{(i,j)}(x,y)dxdy,\ l=0,\ldots,\frac{(\ell+1)(\ell+2)}{2}-1. \tag{3.2}$$

Remark 1. The construction of different polynomials $q_\ell(x,y),\ell=0,\ldots,k$ is very simple, because of the application of the local orthonormal basis over $I_{i,j}$. Since the two-dimensional solution $u_h(x,y,t)\in W_h^k$ is written in (2.8), we can directly obtain $q_\ell(x,y)=\sum_{l=0}^{\frac{(\ell+1)(\ell+2)}{2}-1}u_{i,j}^{(l)}(t)v_l^{(i,j)}(x,y),\ell=0,\ldots,k$, respectively.

Step 1.2. Obtain equivalent expressions for these constructed polynomials of different degrees. To keep consistent notation, we will denote $p_{0,1}(x,y)=q_0(x,y)$. For different high-order approximations, following similar ideas for classical CWENO schemes [4,22,23] and in [40,41], we obtain polynomials $p_{\ell,\ell}(x,y),\ \ell=1,\ldots,k$ through

$$p_{\ell,\ell}(x,y)=\frac{1}{\gamma_{\ell,\ell}}q_\ell(x,y)-\frac{\gamma_{\ell-1,\ell}}{\gamma_{\ell,\ell}}p_{\ell-1,\ell}(x,y),\ \ell=1,\ldots,k, \tag{3.3}$$

with $\gamma_{\ell-1,\ell}+\gamma_{\ell,\ell}=1$ and $\gamma_{\ell,\ell}\neq 0$, together with polynomials $p_{\ell,\ell+1}(x,y),\ \ell=1,\ldots,k-1$ through

$$p_{\ell,\ell+1}(x,y)=\omega_{\ell,\ell}p_{\ell,\ell}(x,y)+\omega_{\ell-1,\ell}p_{\ell-1,\ell}(x,y),\ell=1,\ldots,k-1, \tag{3.4}$$

with $\omega_{\ell-1,\ell}+\omega_{\ell,\ell}=1$.

Step 1.3. Compute the smoothness indicators β_{ℓ,ℓ_2}, which measure how smooth the functions $p_{\ell,\ell_2}(x,y)$ for $\ell=\ell_2-1$, ℓ_2; $\ell_2=1,2,3,4$ are in the interval $I_{i,j}$. We use the same recipe for the smoothness indicators as in [19,34]:

$$\beta_{\ell,\ell_2}=\sum_{|\alpha|=1}^{\kappa}\int_{I_{i,j}}\left(\Delta x_i\Delta y_j\right)^{|\alpha|-1}\left(\frac{\partial^{|\alpha|}}{\partial x^{\alpha_1}\partial y^{\alpha_2}}p_{\ell,\ell_2}(x,y)\right)^2 dxdy,\ \ell=\ell_2-1,\ell_2;\ \ell_2=1,2,3,4, \tag{3.5}$$

where $\kappa=\ell$, $\alpha=(\alpha_1,\alpha_2)$, and $|\alpha|=\alpha_1+\alpha_2$, respectively. The only exception is $\beta_{0,1}$, which we magnify from zero to a value defined below. We first denote the linear polynomial $q_{i,j-1}(x,y)$ with the L^2 projection methodology of $u_h(x,y)\in W_h^k=\{v(x,y):v(x,y)|_{I_{i,j-1}}\in\mathbb{P}^k(I_{i,j-1})\}$ satisfying

$$\int_{I_{i,j-1}} q_{i,j-1}(x,y)v_l^{(i,j-1)}(x,y)dxdy=\int_{I_{i,j-1}} u_h(x,y)v_l^{(i,j-1)}(x,y)dxdy,\ l=0,1,2, \tag{3.6}$$

the linear polynomial $q_{i,j+1}(x,y)$ with the L^2 projection methodology of $u_h(x,y)\in W_h^k=\{v(x,y):v(x,y)|_{I_{i,j+1}}\in\mathbb{P}^k(I_{i,j+1})\}$ satisfying

$$\int_{I_{i,j+1}} q_{i,j+1}(x,y)v_l^{(i,j+1)}(x,y)dxdy=\int_{I_{i,j+1}} u_h(x,y)v_l^{(i,j+1)}(x,y)dxdy,\ l=0,1,2, \tag{3.7}$$

the linear polynomial $q_{i-1,j}(x,y)$ with the L^2 projection methodology of $u_h(x,y)\in W_h^k=\{v(x,y):v(x,y)|_{I_{i-1,j}}\in\mathbb{P}^k(I_{i-1,j})\}$ satisfying

$$\int_{I_{i-1,j}} q_{i-1,j}(x,y)v_l^{(i-1,j)}(x,y)dxdy=\int_{I_{i-1,j}} u_h(x,y)v_l^{(i-1,j)}(x,y)dxdy,\ l=0,1,2, \tag{3.8}$$

and the linear polynomial $q_{i+1,j}(x,y)$ with the L^2 projection methodology of $u_h(x,y)\in W_h^k=\{v(x,y):v(x,y)|_{I_{i+1,j}}\in\mathbb{P}^k(I_{i+1,j})\}$ satisfying

$$\int_{I_{i+1,j}} q_{i+1,j}(x,y)v_l^{(i+1,j)}(x,y)dxdy=\int_{I_{i+1,j}} u_h(x,y)v_l^{(i+1,j)}(x,y)dxdy,\ l=0,1,2. \tag{3.9}$$

Remark 2. Since the two-dimensional solution $u_h(x,y,t)\in W_h^k$ is written in (2.8), we can obtain $q_{i,j-1}(x,y)=\sum_{l=0}^{2}u_{i,j-1}^{(l)}(t)v_l^{(i,j-1)}(x,y)$, $q_{i,j+1}(x,y)=\sum_{l=0}^{2}u_{i,j+1}^{(l)}(t)v_l^{(i,j+1)}(x,y)$, $q_{i-1,j}(x,y)=\sum_{l=0}^{2}u_{i-1,j}^{(l)}(t)v_l^{(i-1,j)}(x,y)$, and $q_{i,j+1}(x,y)=\sum_{l=0}^{2}u_{i,j+1}^{(l)}(t)v_l^{(i,j+1)}(x,y)$, respectively.

Then the associated smoothness indicators are

$$\varsigma_{i,j-1}=\int_{I_{i,j}}\left(\frac{\partial}{\partial x}q_{i,j-1}(x,y)\right)^2+\left(\frac{\partial}{\partial y}q_{i,j-1}(x,y)\right)^2 dxdy, \tag{3.10}$$

$$\varsigma_{i,j+1}=\int_{I_{i,j}}\left(\frac{\partial}{\partial x}q_{i,j+1}(x,y)\right)^2+\left(\frac{\partial}{\partial y}q_{i,j+1}(x,y)\right)^2 dxdy, \tag{3.11}$$

$$\varsigma_{i-1,j}=\int_{I_{i,j}}\left(\frac{\partial}{\partial x}q_{i-1,j}(x,y)\right)^2+\left(\frac{\partial}{\partial y}q_{i-1,j}(x,y)\right)^2 dxdy, \tag{3.12}$$

and

$$\varsigma_{i+1,j}=\int_{I_{i,j}}\left(\frac{\partial}{\partial x}q_{i+1,j}(x,y)\right)^2+\left(\frac{\partial}{\partial y}q_{i+1,j}(x,y)\right)^2 dxdy. \tag{3.13}$$

After that, we define $\beta_{0,1}$ as

$$\beta_{0,1}=\min(\varsigma_{i,j-1},\varsigma_{i,j+1},\varsigma_{i-1,j},\varsigma_{i+1,j}). \tag{3.14}$$

Step 1.4. Compute the nonlinear weights based on the linear weights and the smoothness indicators. We adopt the WENO-Z recipe as shown in [2,5], with τ_{ℓ_2} for $\ell_2 = 1, 2, 3, 4$ defined as related to the absolute difference between the smoothness indicators:

$$\tau_{\ell_2} = \left(\beta_{\ell_2,\ell_2} - \beta_{\ell_2-1,\ell_2}\right)^2, \quad \ell_2 = 1, 2, 3, 4. \tag{3.15}$$

The nonlinear weights are then given as

$$\omega_{\ell_1,\ell_2} = \frac{\bar{\omega}_{\ell_1,\ell_2}}{\sum_{\ell=1}^{\ell_2} \bar{\omega}_{\ell,\ell_2}}, \ \bar{\omega}_{\ell_1,\ell_2} = \gamma_{\ell_1,\ell_2}\left(1 + \frac{\tau_{\ell_2}}{\varepsilon + \beta_{\ell_1,\ell_2}}\right), \ \ell_1 = \ell_2 - 1, \ell_2; \ \ell_2 = 1, 2, 3, 4. \tag{3.16}$$

Here ε is taken as 10^{-10} in all simulations.

Step 1.5. The new final reconstruction polynomial $u_h^{new}|_{I_{i,j}} = p^{new}(x, y)$ on the troubled cell $I_{i,j}$ is given by

$$p^{new}(x, y) = \sum_{\ell=\ell_2-1}^{\ell_2} \omega_{\ell,\ell_2} p_{\ell,\ell_2}(x, y), \quad \ell_2 = 1, 2, 3, 4, \tag{3.17}$$

for the second-order, third-order, fourth-order, or fifth-order approximations, respectively.

Then we present the details of the multi-resolution WENO limiting procedure for two-dimensional systems. Consider (1.2) where u, $f(u)$, and $g(u)$ are vectors with m components. In order to achieve better non-oscillatory qualities, the multi-resolution WENO reconstruction limiter is used with a local characteristic field decomposition. In this paper, we only consider the following Euler system with $m = 4$:

$$\frac{\partial}{\partial t}\begin{pmatrix} \rho \\ \rho\mu \\ \rho\nu \\ E \end{pmatrix} + \frac{\partial}{\partial x}\begin{pmatrix} \rho\mu \\ \rho\mu^2 + p \\ \rho\mu\nu \\ \mu(E + p) \end{pmatrix} + \frac{\partial}{\partial y}\begin{pmatrix} \rho\nu \\ \rho\mu\nu \\ \rho\nu^2 + p \\ \nu(E + p) \end{pmatrix} = 0, \tag{3.18}$$

where ρ is the density, μ is the x-direction velocity, ν is the y-direction velocity, E is the total energy, p is the pressure, and $\gamma = 1.4$ in our test cases. We then give the left and right eigenvector matrices of Jacobian matrices $f'(u)$ and $g'(u)$ as $L_{ij}^x(u)$, $R_{ij}^x(u)$, $L_{ij}^y(u)$, and $R_{ij}^y(u)$ in [45], respectively. The troubled cell $I_{i,j}$ is detected by the new modified version of the classical KXRCF shock detection technique [20]. Denote p_ℓ, $\ell = 0, \ldots, 4$ to be the associated polynomial vectors of different degrees. Then we perform the characteristic-wise multi-resolution WENO limiting procedure as follows:

Step 2.1. Compute the new polynomial vectors $p^{x,new}$ and $p^{y,new}$ by using the characteristic-wise multi-resolution WENO limiting procedure:

Step 2.1.1. Compute $L_{i,j}^x = L_{i,j}^x(\bar{u}_{i,j})$, $L_{i,j}^y = L_{i,j}^y(\bar{u}_{i,j})$, $R_{i,j}^x = R_{i,j}^x(\bar{u}_{i,j})$, and $R_{i,j}^y = R_{i,j}^x(\bar{u}_{i,j})$ as specified in [45], where again $\bar{u}_{i,j}$ is the cell average of u on the troubled cell $I_{i,j}$.

Step 2.1.2. Project the polynomial vectors p_ℓ, $\ell = 0, \ldots, 4$, into the characteristic fields $\tilde{\tilde{p}}_\ell^x = L_{i,j}^x p_\ell$ and $\tilde{\tilde{p}}_\ell^y = L_{i,j}^y p_\ell$, $\ell = 0, \ldots, 4$, each of them being a four-component vector, and each component of the vector is a k-th degree polynomial.

Step 2.1.3. Perform Step 1.1 to Step 1.5 of the multi-resolution WENO limiting procedure that has been specified for the scalar case, to obtain the new four-component vectors on the troubled cell $I_{i,j}$ denoted by $\tilde{\tilde{p}}^{x,new}$ and $\tilde{\tilde{p}}^{y,new}$.

Step 2.1.4. Project $\tilde{\tilde{p}}^{x,new}$ and $\tilde{\tilde{p}}^{y,new}$ into the physical space $p^{x,new} = R_{i,j}^x \tilde{\tilde{p}}^{x,new}$ and $p^{y,new} = R_{i,j}^y \tilde{\tilde{p}}^{y,new}$, respectively.

Step 2.2. The final new four-component vector on the troubled cell $I_{i,j}$ is defined as $u_h^{new}|_{I_{i,j}} = \dfrac{p^{x,new} + p^{y,new}}{2}$.

4. Numerical results

In this section, we provide numerical results to demonstrate the performance of the new type of multi-resolution WENO limiters for second-order, third-order, fourth-order, and fifth-order RKDG methods described in previous sections. The simple Lax-Friedrichs flux is used in all numerical examples. The CFL number is 0.3 for the second-order (P^1), 0.18 for the third-order (P^2), 0.1 for the fourth-order (P^3), and 0.08 for the fifth-order (P^4) RKDG methods both in one and two dimensions, except for the accuracy examples where the time step is smaller so as to guarantee that the spatial error dominates. We define all cells as troubled cells in Example 4.1 and Example 4.2, so as to test numerical accuracy when the new type of multi-resolution WENO reconstruction procedure is artificially enacted on all cells. Then we set the constant C_k in (3.1) to be 1 in other examples, unless specified otherwise.

Example 4.1. We solve the following scalar Burgers' equation in two dimensions:

$$\mu_t + \left(\frac{\mu^2}{2}\right)_x + \left(\frac{\mu^2}{2}\right)_y = 0, \ (x, y) \in [0, 4] \times [0, 4], \tag{4.1}$$

Table 4.1
$\mu_t + \left(\frac{\mu^2}{2}\right)_x + \left(\frac{\mu^2}{2}\right)_y = 0$. $\mu(x, y, 0) = 0.5 + \sin(\pi(x+y)/2)$. Periodic boundary condition. $T = 0.5/\pi$. L^1 and L^∞ errors. RKDG with multi-resolution WENO limiter compared to RKDG without limiter.

	Cells	DG with multi-resolution WENO limiter				DG without limiter			
		L^1 error	order	L^∞ error	order	L^1 error	order	L^∞ error	order
P^1	10 × 10	3.77E−2		3.72E−1		3.19E−2		3.40E−1	
	20 × 20	8.86E−3	2.09	1.12E−1	1.72	7.88E−3	2.02	1.05E−1	1.68
	40 × 40	1.97E−3	2.16	3.26E−2	1.79	1.98E−3	1.99	3.26E−2	1.69
	80 × 80	4.92E−4	2.01	9.16E−3	1.83	4.92E−4	2.01	9.16E−3	1.83
	160 × 160	1.23E−4	2.00	2.40E−3	1.93	1.23E−4	2.00	2.40E−3	1.93
P^2	10 × 10	7.37E−3		1.90E−1		5.20E−3		1.81E−1	
	20 × 20	1.19E−3	2.63	4.20E−2	2.18	8.29E−4	2.64	4.15E−2	2.12
	40 × 40	1.50E−4	2.99	6.03E−3	2.80	1.12E−4	2.88	6.03E−3	2.78
	80 × 80	1.64E−5	3.19	1.00E−3	2.59	1.44E−5	2.96	1.00E−3	2.59
	160 × 160	1.83E−6	3.17	1.37E−4	2.87	1.82E−6	2.98	1.37E−4	2.86
P^3	10 × 10	2.92E−3		6.91E−2		1.91E−3		8.29E−2	
	20 × 20	8.41E−4	1.80	1.00E−2	2.78	1.29E−4	3.89	9.21E−3	3.17
	40 × 40	7.58E−5	3.47	1.11E−3	3.17	9.11E−6	3.82	7.51E−4	3.61
	80 × 80	5.76E−7	7.04	6.03E−5	4.21	5.76E−7	3.98	6.03E−5	3.64
	160 × 160	3.65E−8	3.98	3.97E−6	3.92	3.65E−8	3.98	3.97E−6	3.92
P^4	10 × 10	3.68E−3		4.11E−2		3.77E−4		1.95E−2	
	20 × 20	8.35E−4	2.14	7.80E−3	2.40	2.50E−5	3.91	2.96E−3	2.72
	40 × 40	1.00E−6	9.70	1.16E−4	6.07	9.71E−7	4.69	1.16E−4	4.67
	80 × 80	3.46E−8	4.86	5.60E−6	4.37	3.46E−8	4.81	5.60E−6	4.37
	160 × 160	1.20E−9	4.85	2.09E−7	4.74	1.20E−9	4.85	2.09E−7	4.74

with the initial condition $\mu(x, y, 0) = 0.5 + \sin(\pi(x+y)/2)$ and periodic boundary conditions in both directions. The final time is $t = 0.5/\pi$, when the solution is still smooth. The errors and numerical orders of accuracy for the RKDG methods with the multi-resolution WENO limiters comparing with the original RKDG methods without limiters are shown in Table 4.1. We observe good results as in the one-dimensional case (not shown to save space), even when all cells in the computational field are artificially denoted as troubled cells.

Example 4.2. We solve two-dimensional Euler equations (3.18). The initial conditions are: $\rho(x, y, 0) = 1 + 0.2\sin(\pi(x+y))$, $\mu(x, y, 0) = 0.7$, $\nu(x, y, 0) = 0.3$, and $p(x, y, 0) = 1$. The computational domain is $(x, y) \in [0, 2] \times [0, 2]$. Periodic boundary conditions are applied in both directions. The exact density solution is $\rho(x, y, t) = 1 + 0.2\sin(\pi(x + y - t))$. The final time is $t = 2$. The errors and numerical orders of accuracy of the density for the RKDG methods with the associated multi-resolution WENO limiters comparing with the original RKDG methods without limiters are shown in Table 4.2. The proposed multi-resolution WENO limiters for the RKDG methods again could keep the designed order of accuracy.

We now test the performance of the RKDG methods with the associated multi-resolution WENO limiters for problems containing shock waves or contact discontinuities. We define $C_k = 1$ from now on for the following examples.

Example 4.3. We consider Sod problem [37]:

$$(\rho, \mu, p)^T = \begin{cases} (1, 0, 2.5)^T, & x \in [-5, 0), \\ (0.125, 0, 0.25)^T, & x \in [0, 5]. \end{cases} \tag{4.2}$$

The computed density ρ is plotted at t=2 against the exact solution in Fig. 4.1, a point-wise error between the exact solution and numerical solution of density is shown in Fig. 4.2, and the time history of the troubled cells is shown in Fig. 4.3, respectively. We observe that the new multi-resolution WENO limiters for the RKDG methods of different orders work well in comparison with the exact solution.

Example 4.4. We consider Lax problem [21]: $(\rho, \mu, p)^T = (0.445, 0.698, 3.528)^T$ for $x \in [-5, 0)$; $(\rho, \mu, p)^T = (0.5, 0, 0.571)^T$ for $x \in [0, 5]$. The computed density ρ is plotted at t=1.3 against the exact solution in Fig. 4.4, a point-wise error between the exact solution and numerical solution of density is shown in Fig. 4.5, and the time history of the troubled cells is shown in Fig. 4.6, respectively. We observe that the RKDG methods of different orders with multi-resolution WENO limiters perform well in comparison with the exact solution.

Example 4.5. A higher order scheme would show its advantage when the solution contains both shocks and complex smooth region structures. A typical example for this is the problem of shock interaction with entropy waves [36]. We solve the shock density wave interaction problem with a moving Mach = 3 shock interacting with sine waves in density:

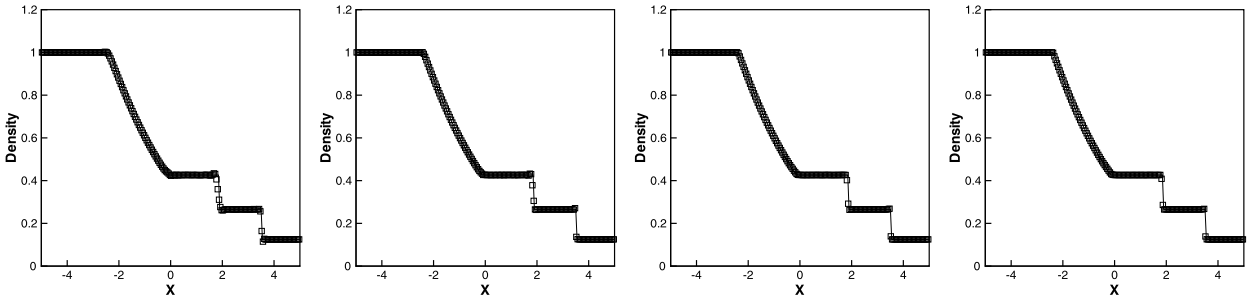

Fig. 4.1. The Sod problem. RKDG methods with multi-resolution WENO limiters. Solid line: the exact solution; squares: numerical solution. From left to right: second-order (P^1), third-order (P^2), fourth-order (P^3), and fifth-order (P^4). Cells: 200.

Table 4.2
2D-Euler equations: initial data $\rho(x, y, 0) = 1 + 0.2\sin(\pi(x + y))$, $\mu(x, y, 0) = 0.7$, $v(x, y, 0) = 0.3$, and $p(x, y, 0) = 1$. Periodic boundary condition. $T = 2.0$. L^1 and L^∞ errors. RKDG with multi-resolution WENO limiter compared to RKDG without limiter.

	Cells	DG with multi-resolution WENO limiter				DG without limiter			
		L^1 error	order	L^∞ error	order	L^1 error	order	L^∞ error	order
	50 × 50	2.93E−4		1.06E−3		2.93E−4		1.06E−3	
	60 × 60	1.84E−4	2.55	7.84E−4	1.67	1.84E−4	2.55	7.85E−4	1.67
P^1	70 × 70	1.26E−4	2.47	5.99E−4	1.74	1.26E−4	2.47	6.00E−4	1.75
	80 × 80	9.14E−5	2.41	4.73E−4	1.78	9.14E−5	2.41	4.73E−4	1.78
	90 × 90	6.92E−5	2.36	3.82E−4	1.82	6.92E−5	2.36	3.82E−4	1.82
	100 × 100	5.42E−5	2.32	3.15E−4	1.83	5.42E−5	2.32	3.15E−4	1.83
	50 × 50	6.91E−6		6.75E−5		6.33E−6		6.75E−5	
	60 × 60	3.78E−6	3.30	3.97E−5	2.91	3.61E−6	3.07	3.97E−5	2.91
P^2	70 × 70	2.27E−6	3.32	2.52E−5	2.93	2.25E−6	3.07	2.52E−5	2.93
	80 × 80	1.50E−6	3.09	1.70E−5	2.95	1.49E−6	3.06	1.70E−5	2.95
	90 × 90	1.04E−6	3.09	1.20E−5	2.96	1.04E−6	3.06	1.20E−5	2.96
	100 × 100	7.57E−7	3.06	8.81E−6	2.97	7.57E−7	3.05	8.81E−6	2.97
	50 × 50	7.15E−8		1.02E−6		7.15E−8		1.02E−6	
	60 × 60	3.44E−8	4.02	4.92E−7	4.00	3.44E−8	4.02	4.92E−7	4.00
P^3	70 × 70	1.85E−8	4.01	2.65E−7	4.00	1.85E−8	4.01	2.65E−7	4.00
	80 × 80	1.08E−8	4.01	1.55E−7	4.00	1.08E−8	4.01	1.55E−7	4.00
	90 × 90	6.77E−9	4.00	9.71E−8	4.00	6.77E−9	4.00	9.71E−8	4.00
	100 × 100	4.44E−9	4.00	6.37E−8	4.00	4.44E−9	4.00	6.37E−8	4.00
	50 × 50	1.62E−9		2.80E−8		1.62E−9		2.80E−8	
	60 × 60	6.54E−10	4.99	1.13E−8	4.96	6.54E−10	4.99	1.13E−8	4.96
P^4	70 × 70	3.02E−10	5.00	5.29E−9	4.97	3.02E−10	5.00	5.29E−9	4.97
	80 × 80	1.55E−10	5.00	2.72E−9	4.97	1.55E−10	5.00	2.72E−9	4.97
	90 × 90	8.61E−11	5.00	1.51E−9	4.98	8.61E−11	5.00	1.51E−9	4.98
	100 × 100	5.08E−11	5.00	8.96E−10	4.98	5.08E−11	5.00	8.96E−10	4.98

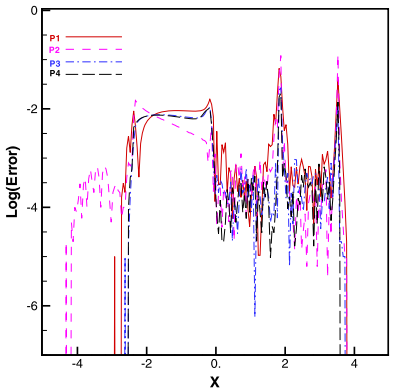

Fig. 4.2. The Sod problem. RKDG methods with multi-resolution WENO limiters. Error shows the absolute difference of a point-wise error between the exact solution and numerical solution. Different lines correspond to the density results of second-order (P^1), third-order (P^2), fourth-order (P^3), and fifth-order (P^4). Cells: 200.

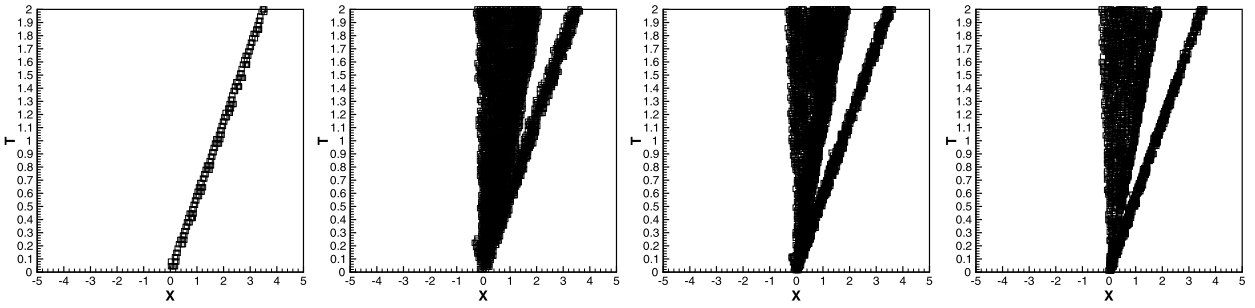

Fig. 4.3. The Sod problem. RKDG methods with multi-resolution WENO limiters. Troubled cells. Squares denote cells which are identified as troubled cells subject to the multi-resolution WENO limiting. From left to right: second-order (P^1), third-order (P^2), fourth-order (P^3), and fifth-order (P^4). Cells: 200.

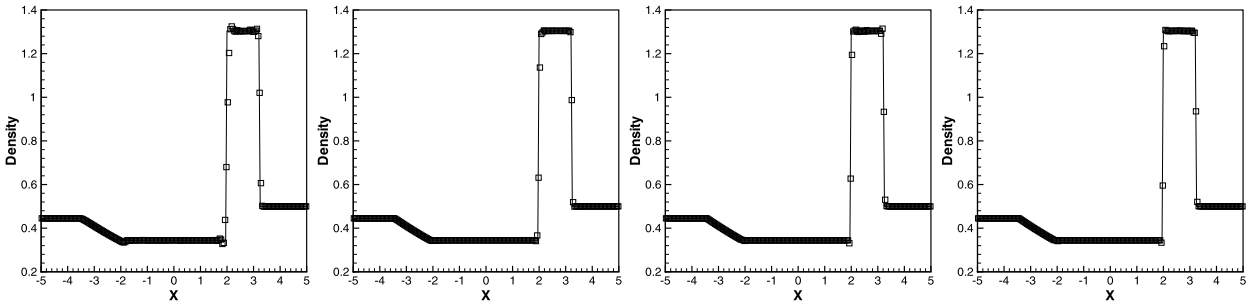

Fig. 4.4. The Lax problem. RKDG methods with multi-resolution WENO limiters. Solid line: the exact solution; squares: numerical solution. From left to right: second-order (P^1), third-order (P^2), fourth-order (P^3), and fifth-order (P^4). Cells: 200.

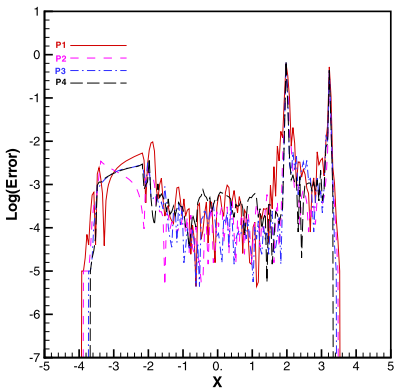

Fig. 4.5. The Lax problem. RKDG methods with multi-resolution WENO limiters. Error shows the absolute difference of a point-wise error between the exact solution and numerical solution. Different lines correspond to the density results of second-order (P^1), third-order (P^2), fourth-order (P^3), and fifth-order (P^4). Cells: 200.

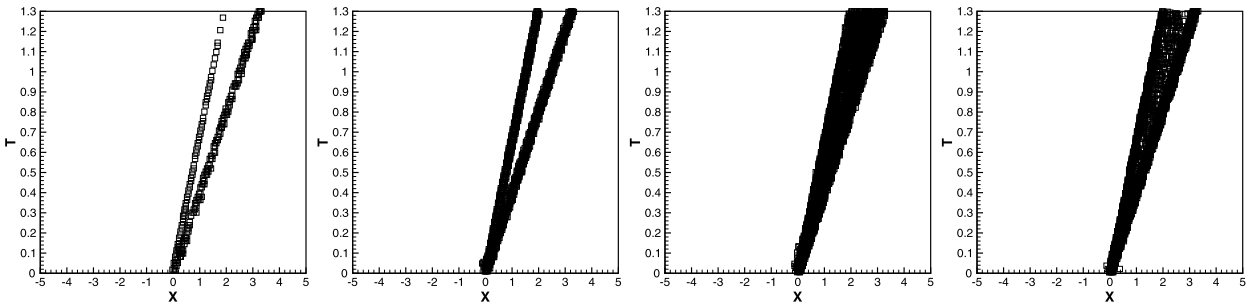

Fig. 4.6. The Lax problem. RKDG methods with multi-resolution WENO limiters. Troubled cells. Squares denote cells which are identified as troubled cells subject to the multi-resolution WENO limiting. From left to right: second-order (P^1), third-order (P^2), fourth-order (P^3), and fifth-order (P^4). Cells: 200.

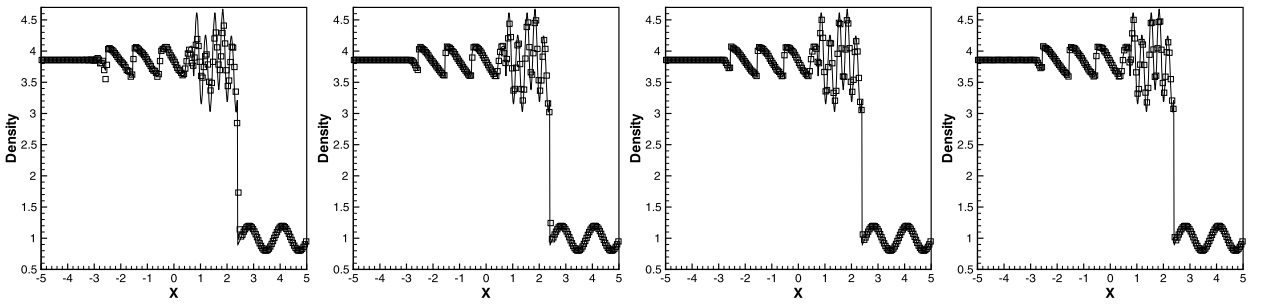

Fig. 4.7. The shock density wave interaction problem. RKDG methods with multi-resolution WENO limiters. Solid line: the "exact" solution; squares: numerical solution. From left to right: second-order (P^1), third-order (P^2), fourth-order (P^3), and fifth-order (P^4). Cells: 200.

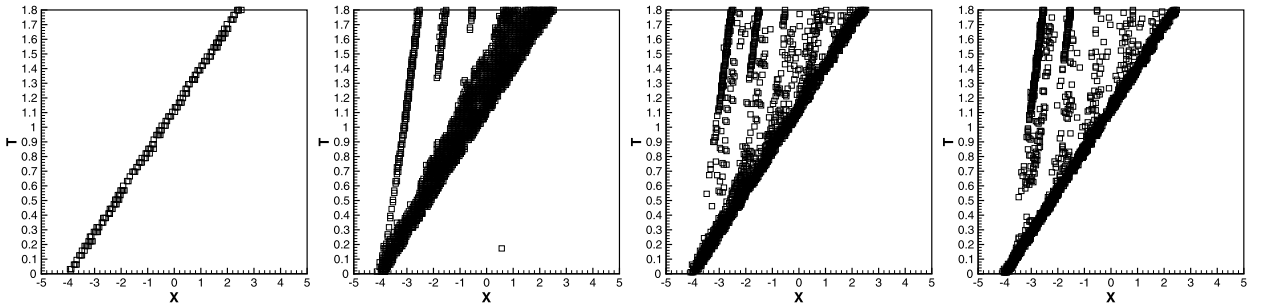

Fig. 4.8. The shock density wave interaction problem. RKDG methods with multi-resolution WENO limiters. Troubled cells. Squares denote cells which are identified as troubled cells subject to the multi-resolution WENO limiting. From left to right: second-order (P^1), third-order (P^2), fourth-order (P^3), and fifth-order (P^4). Cells: 200.

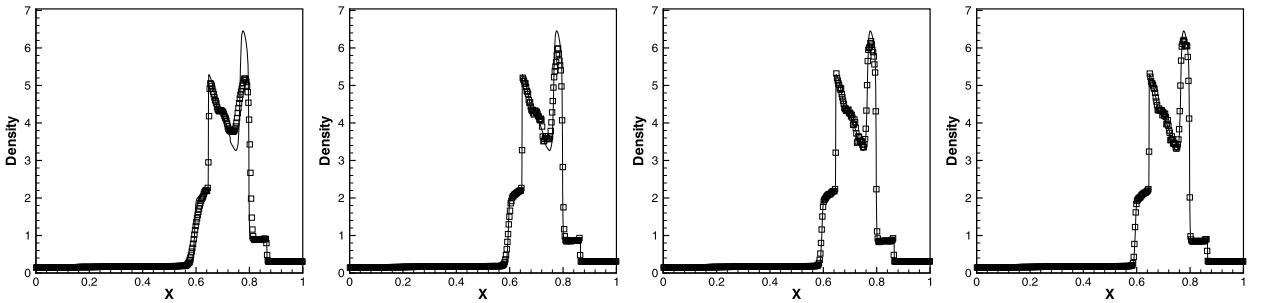

Fig. 4.9. The blast wave problem. RKDG methods with multi-resolution WENO limiters. Solid line: the "exact" solution; squares: numerical solution. From left to right: second-order (P^1), third-order (P^2), fourth-order (P^3), and fifth-order (P^4). Cells: 400.

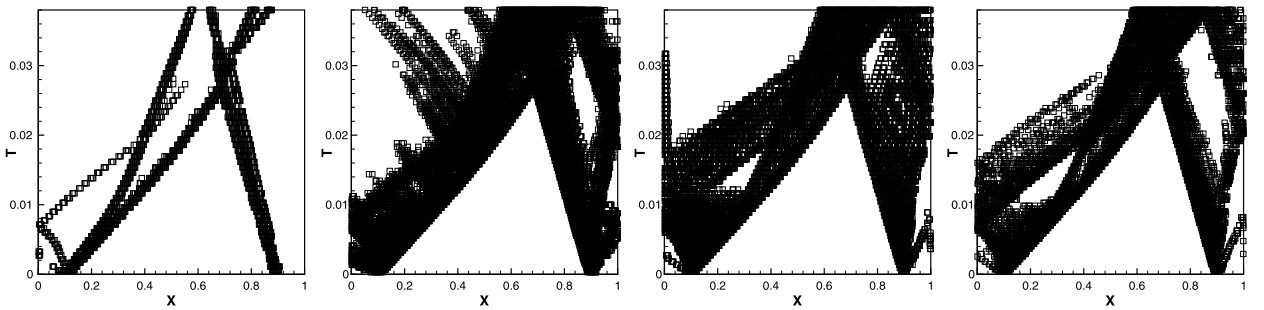

Fig. 4.10. The blast wave problem. RKDG methods with multi-resolution WENO limiters. Troubled cells. Squares denote cells which are identified as troubled cells subject to the multi-resolution WENO limiting. From left to right: second-order (P^1), third-order (P^2), fourth-order (P^3), and fifth-order (P^4). Cells: 400.

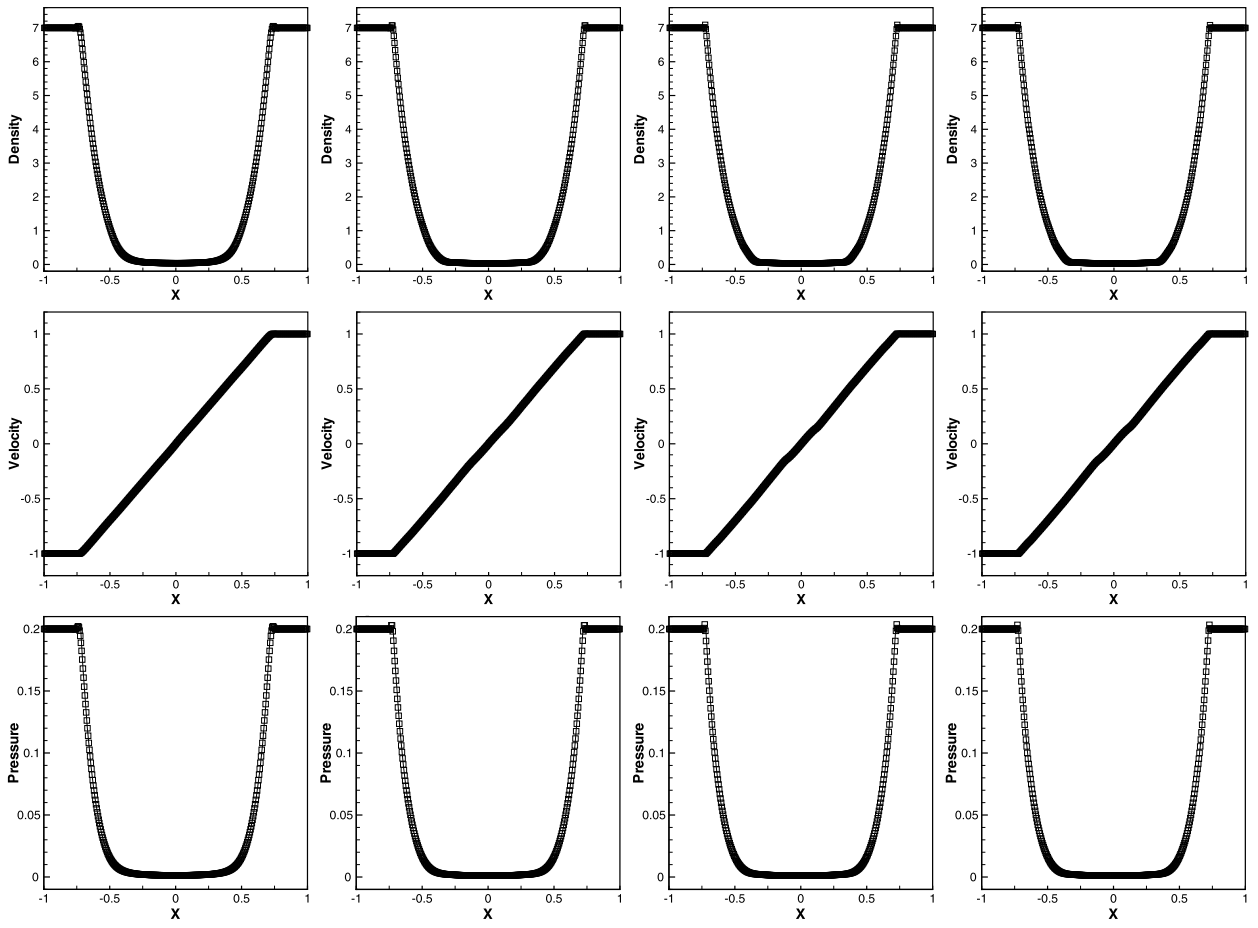

Fig. 4.11. The double rarefaction wave problem. RKDG methods with multi-resolution WENO limiters. From top to bottom: density, velocity, and pressure. Solid line: the exact solution; squares: numerical solution. From left to right: second-order (P^1), third-order (P^2), fourth-order (P^3), and fifth-order (P^4). Cells: 400.

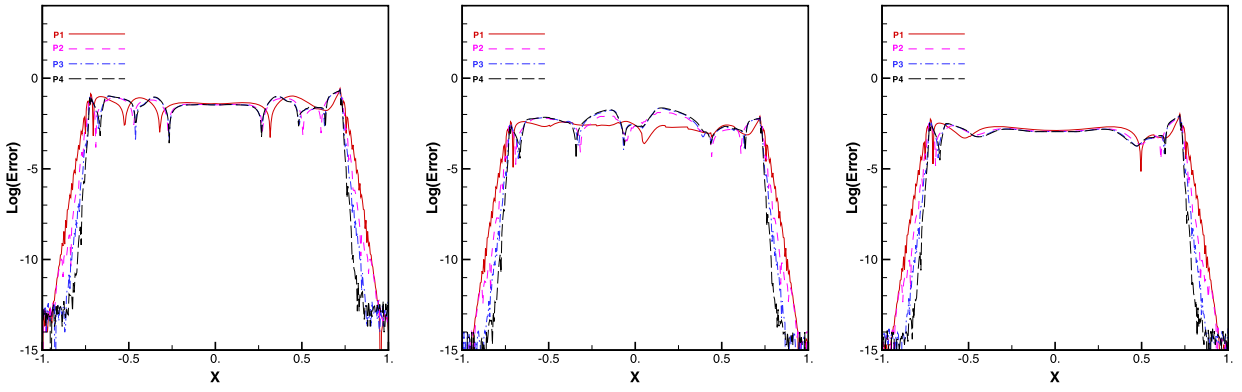

Fig. 4.12. The double rarefaction wave problem. RKDG methods with multi-resolution WENO limiters. Error shows the absolute difference of a point-wise error between the exact solution and numerical solution. From left to right: different lines correspond to the density, velocity, and pressure results of second-order (P^1), third-order (P^2), fourth-order (P^3), and fifth-order (P^4). Cells: 400.

$(\rho, \mu, p)^T = (3.857143, 2.629369, 10.333333)^T$ for $x \in [-5, -4)$; $(\rho, \mu, p)^T = (1 + 0.2\sin(5x), 0, 1)^T$ for $x \in [-4, 5]$. The computed density ρ is plotted at t = 1.8 against the reference "exact" solution which is a converged solution computed by the fifth-order finite difference WENO scheme [19] with 2000 grid points in Fig. 4.7 and the time history of the troubled cells is shown in Fig. 4.8, respectively. We observe that high-order RKDG methods with high-order multi-resolution WENO limiters work better than low-order RKDG methods with same order multi-resolution WENO limiters in comparison with the exact solution.

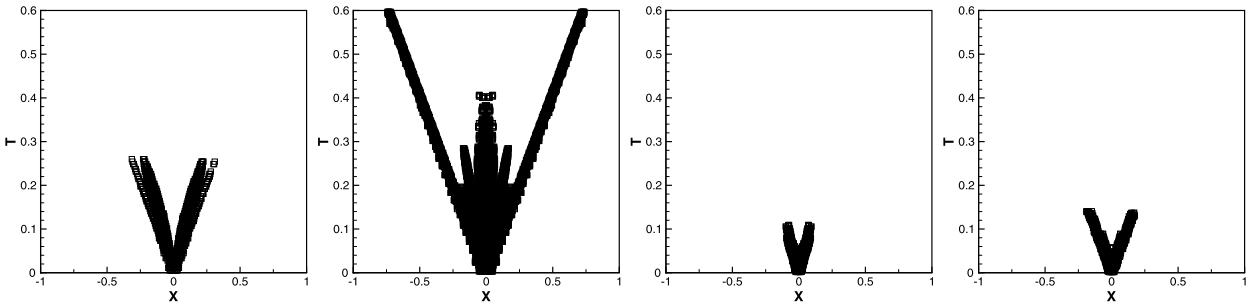

Fig. 4.13. The double rarefaction wave problem. RKDG methods with multi-resolution WENO limiters. Troubled cells. Squares denote cells which are identified as troubled cells subject to the multi-resolution WENO limiting. From left to right: second-order (P^1), third-order (P^2), fourth-order (P^3), and fifth-order (P^4). Cells: 400.

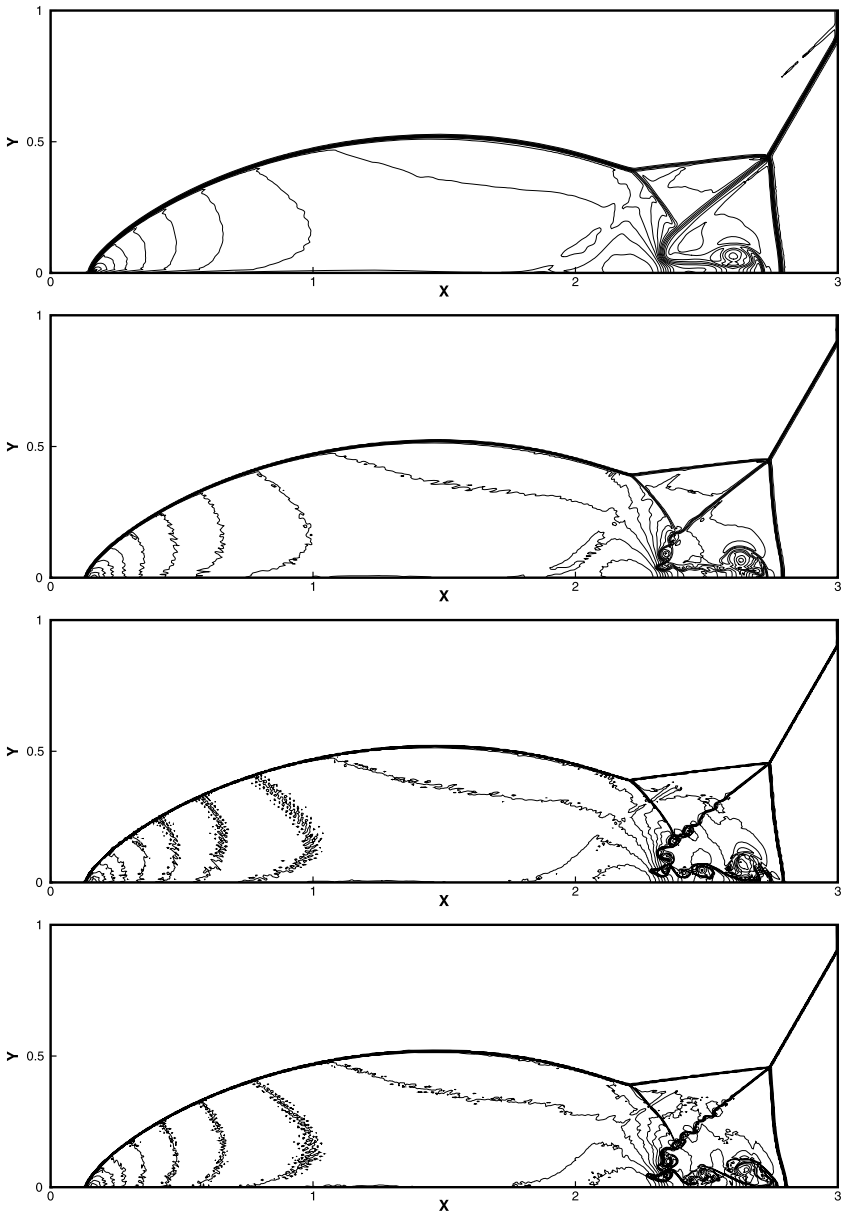

Fig. 4.14. Double Mach refection problem. RKDG methods with multi-resolution WENO limiters. 30 equally spaced density contours from 1.5 to 21.5. From top to bottom: second-order (P^1), third-order (P^2), fourth-order (P^3), and fifth-order (P^4). Cells: 800 $\times$ 200.

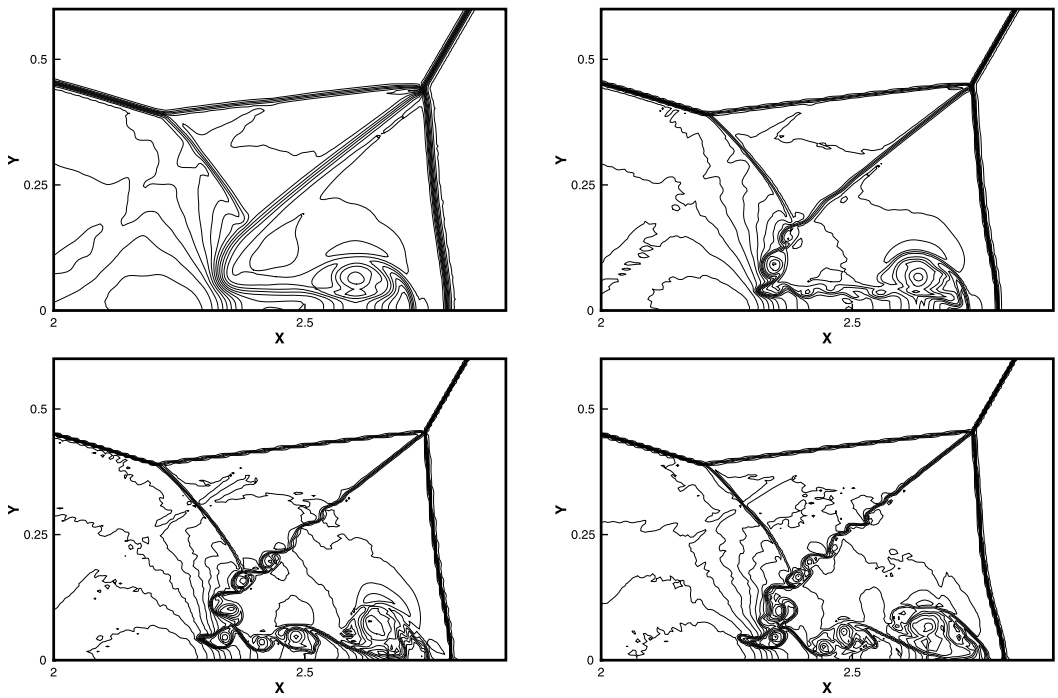

Fig. 4.15. Double Mach refection problem. RKDG methods with multi-resolution WENO limiters. Zoom-in pictures around the Mach stem. 30 equally spaced density contours from 1.5 to 21.5. From left to right and top to bottom: second-order (P^1), third-order (P^2), fourth-order (P^3), and fifth-order (P^4). Cells: 800×200.

Example 4.6. We consider the blast wave problem with the initial conditions [38]: $(\rho, \mu, p)^T = (1, 0, 1000)^T$ for $x \in [0, 0.1)$; $(\rho, \mu, p)^T = (1, 0, 0.01)^T$ for $x \in [0.1, 0.9)$; $(\rho, \mu, p)^T = (1, 0, 100)^T$ for $x \in [0.9, 1.0]$. The computed density ρ is plotted at t = 0.038 against the reference "exact" solution which is a converged solution computed by the fifth-order finite difference WENO scheme [19] with 2000 grid points in Fig. 4.9 and the time history of the troubled cells is shown in Fig. 4.10, respectively. We observe that the RKDG methods of different orders with associated multi-resolution WENO limiters work well with increasingly high-order accuracy.

Example 4.7. The double rarefaction wave problem [24]. This test case has low pressure and low density regions and is difficult to simulate well. The initial conditions are defined as: $(\rho, \mu, p)^T = (7, -1, 0.2)^T$ for $x \in [-1, 0)$; $(\rho, \mu, p)^T = (7, 1, 0.2)^T$ for $x \in [0, 1]$. The final computational time is $t = 0.6$. The computational results including the density, velocity, and pressure pictures are shown in Fig. 4.11. The point-wise errors between the exact solutions and numerical solutions of density, velocity, and pressure are shown in Fig. 4.12, respectively. The time history of the troubled cells is shown in Fig. 4.13. Once again, the second-order, third-order, fourth-order, and fifth-order RKDG methods with new multi-resolution WENO limiters produce good results.

Example 4.8. Double Mach reflection problem. This model problem is originally from [38]. We solve the two-dimensional Euler equations (3.18) in a computational domain of $[0, 4] \times [0, 1]$. The reflection boundary condition is used at the wall, which for the rest of the bottom boundary (the part from $x = 0$ to $x = \frac{1}{6}$), the exact post-shock condition is imposed. At the top boundary is the exact motion of the Mach 10 shock. The final time is $t = 0.2$. RKDG methods of different orders with multi-resolution WENO limiters, $k = 1$, $k = 2$, $k = 3$, and $k = 4$ (second-order, third-order, fourth-order, and fifth-order), are used in the numerical experiments. The simulation results are shown in Fig. 4.14. The "zoomed-in" pictures around the double Mach stem to show more details are given in Fig. 4.15. The troubled cells identified at the last time step are shown in Fig. 4.16. Clearly, the resolution improves with an increasing k on the same mesh level.

Example 4.9. A Mach 3 wind tunnel with a forward-facing step [38]. The setup of the problem is as follows. The wind tunnel is one length unit wide and three length units long. The step is 0.2 length units high and is located 0.6 length units from the left-hand end of the tunnel. The problem is initialized by a right-going Mach 3 flow. Reflective boundary conditions are applied along the wall of the tunnel and inflow/outflow boundary conditions are applied at the entrance/exit. The final time is $t = 4$. In Fig. 4.17, we show 30 equally spaced density contours from 0.32 to 6.15 computed by the second-order, third-order, fourth-order, and fifth-order RKDG methods with multi-resolution WENO limiters, respectively. The troubled cells identified at the last time step are shown in Fig. 4.18. We can clearly observe that the fifth-order RKDG method with

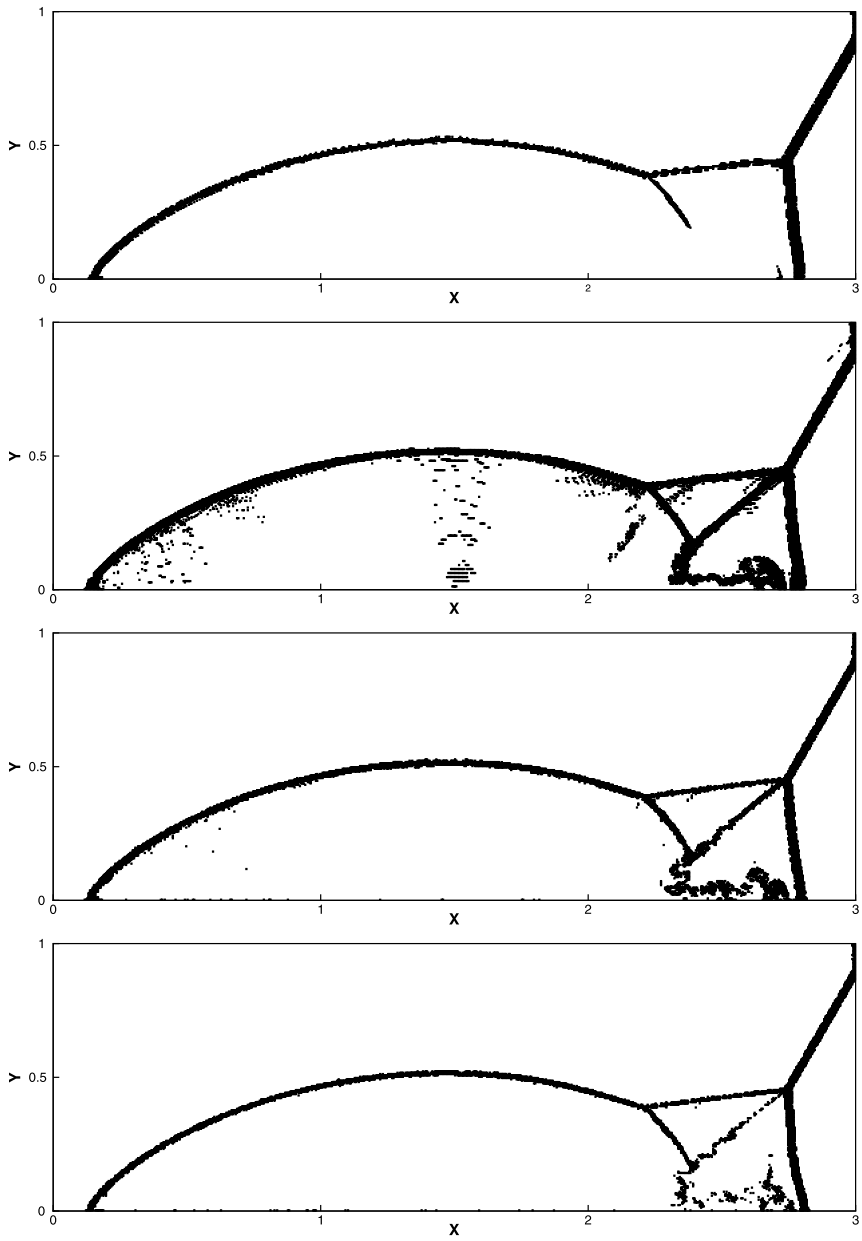

Fig. 4.16. Double Mach refection problem. RKDG methods with multi-resolution WENO limiters. Troubled cells. Squares denote cells which are identified as troubled cells subject to the multi-resolution WENO limiting. From top to bottom: second-order (P^1), third-order (P^2), fourth-order (P^3), and fifth-order (P^4). Cells: 800 $\times$ 200.

multi-resolution WENO limiter gives better resolution than the lower order schemes, especially for the resolution of the physical instability and roll-up of the contact line.

5. Concluding remarks

We have designed a new type of multi-resolution WENO limiters, based on the spatial reconstruction procedure designed in [43], for general Runge-Kutta discontinuous Galerkin (RKDG) methods (second- through fifth-order schemes have been worked out as examples) to solve one-dimensional and two-dimensional hyperbolic conservation laws on structured meshes. The general framework of such multi-resolution WENO limiters for high-order RKDG methods is to first use a new modified version of the KXRCF shock detection technique [20] to detect troubled cells subject to the multi-resolution WENO limiting procedure, then to construct a sequence of hierarchical L^2 projection polynomial solutions of the DG methods completely restricted to the troubled cell itself in a WENO fashion. The main novelty of this paper is the new multi-resolution WENO re-

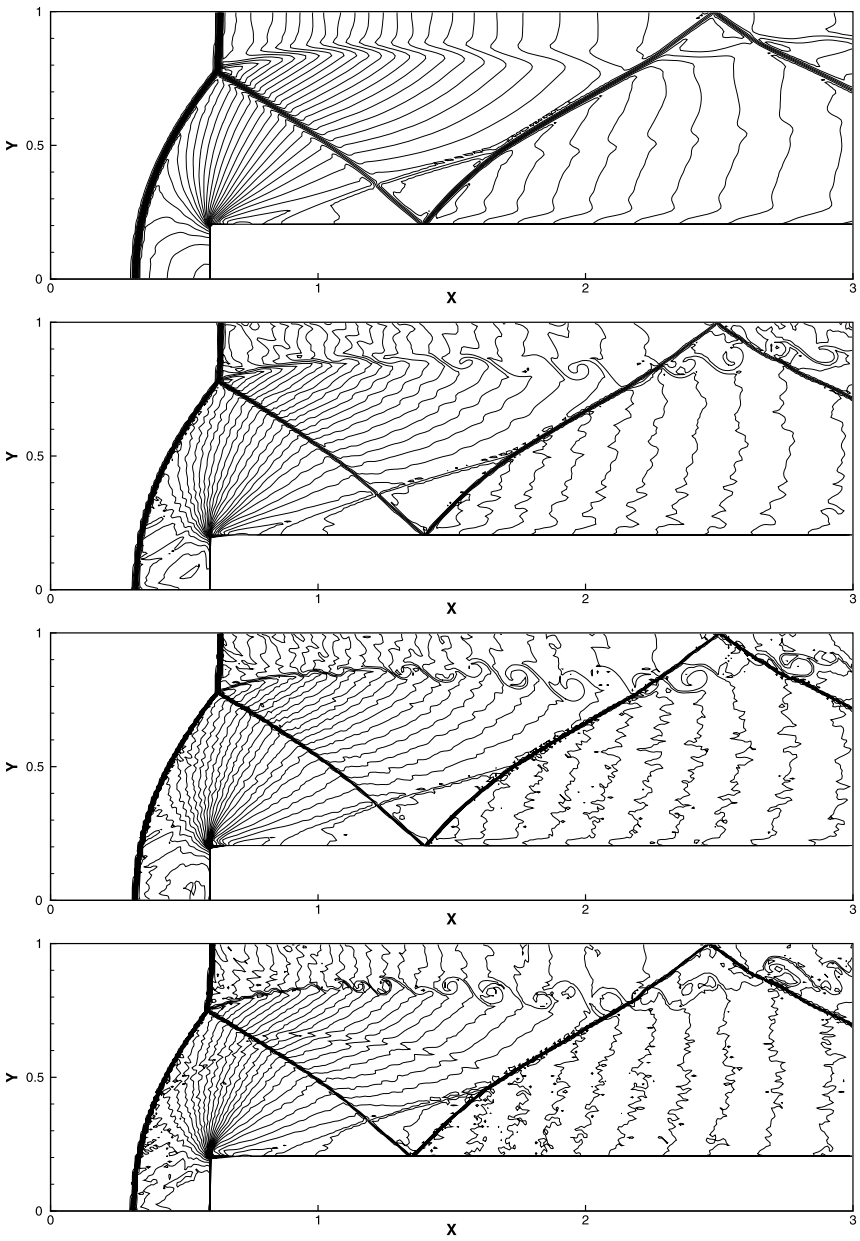

Fig. 4.17. Forward step problem. RKDG methods with multi-resolution WENO limiters. 30 equally spaced density contours from 0.32 to 6.15. From top to bottom: second-order (P^1), third-order (P^2), fourth-order (P^3), and fifth-order (P^4). Cells: 300×100.

construction procedure, which essentially only uses the information defined within the troubled cell itself, with information from neighboring cells used only marginally (when introducing the smoothness indicator of the zeroth order polynomial in the hierarchy), and with simple positive linear weights in the spatial reconstruction procedure. This new spatial reconstruction methodology is simpler, more robust, and could lead to better resolutions for benchmark time-dependent problems containing rarefaction waves, shock waves, and contact discontinuities, than other WENO type limiters for the RKDG methods. The framework of this new type of multi-resolution WENO limiters for arbitrary high-order RKDG methods would be particularly efficient and simple on unstructured meshes including triangular meshes in 2D [44] and tetrahedral meshes in 3D, the study of which is our ongoing work.

Declaration of competing interest

The authors declare that they have no known competing financial interests or personal relationships that could have appeared to influence the work reported in this paper.

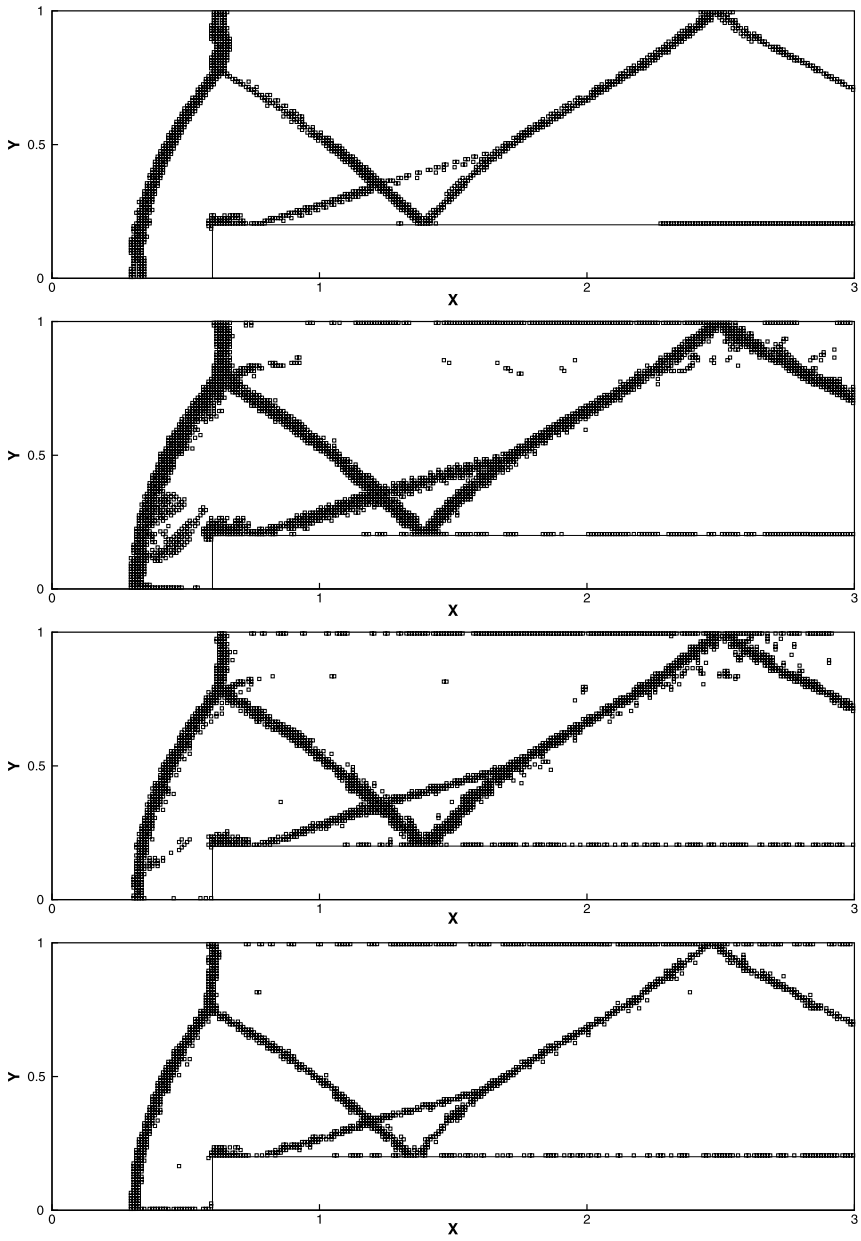

Fig. 4.18. Forward step problem. RKDG methods with multi-resolution WENO limiters. Troubled cells. Squares denote cells which are identified as troubled cells subject to the multi-resolution WENO limiting. From top to bottom: second-order (P^1), third-order (P^2), fourth-order (P^3), and fifth-order (P^4). Cells: 300×100.

References

[1] R. Biswas, K.D. Devine, J. Flaherty, Parallel, adaptive finite element methods for conservation laws, Appl. Numer. Math. 14 (1994) 255–283.
[2] R. Borges, M. Carmona, B. Costa, W.S. Don, An improved weighted essentially non-oscillatory scheme for hyperbolic conservation laws, J. Comput. Phys. 227 (2008) 3191–3211.
[3] A. Burbeau, P. Sagaut, C.H. Bruneau, A problem-independent limiter for high-order Runge-Kutta discontinuous Galerkin methods, J. Comput. Phys. 169 (2001) 111–150.
[4] G. Capdeville, A central WENO scheme for solving hyperbolic conservation laws on non-uniform meshes, J. Comput. Phys. 227 (2008) 2977–3014.
[5] M. Castro, B. Costa, W.S. Don, High order weighted essentially non-oscillatory WENO-Z schemes for hyperbolic conservation laws, J. Comput. Phys. 230 (2011) 1766–1792.
[6] B. Cockburn, S. Hou, C.-W. Shu, The Runge-Kutta local projection discontinuous Galerkin finite element method for conservation laws IV: the multidimensional case, Math. Comput. 54 (1990) 545–581.
[7] B. Cockburn, S.-Y. Lin, C.-W. Shu, TVB Runge-Kutta local projection discontinuous Galerkin finite element method for conservation laws III: one dimensional systems, J. Comput. Phys. 84 (1989) 90–113.

[8] B. Cockburn, C.-W. Shu, TVB Runge-Kutta local projection discontinuous Galerkin finite element method for conservation laws II: general framework, Math. Comput. 52 (1989) 411–435.
[9] B. Cockburn, C.-W. Shu, The Runge-Kutta local projection P^1-discontinuous Galerkin finite element method for scalar conservation laws, RAIRO Model. Math. Anal. Numer. 25 (1991) 337–361.
[10] B. Cockburn, C.-W. Shu, The Runge-Kutta discontinuous Galerkin method for conservation laws V: multidimensional systems, J. Comput. Phys. 141 (1998) 199–224.
[11] O. Friedrichs, Weighted essentially non-oscillatory schemes for the interpolation of mean values on unstructured grids, J. Comput. Phys. 144 (1998) 194–212.
[12] G.S. Fu, C.-W. Shu, A new troubled-cell indicator for discontinuous Galerkin methods for hyperbolic conservation laws, J. Comput. Phys. 347 (2017) 305–327.
[13] A. Harten, Multi-resolution Analysis for ENO Schemes, Institute for Computer Applications in Science and Engineering, NASA Langley Research Center, Hampton, Virginia, September 1991, 23665-5225, Contract No. NAS1-18605.
[14] A. Harten, Discrete multi-resolution analysis and generalized wavelets, Appl. Numer. Math. 12 (1993) 153–192.
[15] A. Harten, Adaptive multiresolution schemes for shock computations, Comput. Phys. 115 (1994) 319–338.
[16] A. Harten, Multiresolution algorithms for the numerical solution of hyperbolic conservation laws, Commun. Pure Appl. Math. 48 (1995) 1305–1342.
[17] A. Harten, Multiresolution representation of data: a general framework, SIAM J. Numer. Anal. 33 (1996) 1205–1256.
[18] C. Hu, C.-W. Shu, Weighted essentially non-oscillatory schemes on triangular meshes, J. Comput. Phys. 150 (1999) 97–127.
[19] G. Jiang, C.-W. Shu, Efficient implementation of weighted ENO schemes, J. Comput. Phys. 126 (1996) 202–228.
[20] L. Krivodonova, J. Xin, J.-F. Remacle, N. Chevaugeon, J.E. Flaherty, Shock detection and limiting with discontinuous Galerkin methods for hyperbolic conservation laws, Appl. Numer. Math. 48 (2004) 323–338.
[21] P.D. Lax, Weak solutions of nonlinear hyperbolic equations and their numerical computation, Commun. Pure Appl. Math. 7 (1954) 159–193.
[22] D. Levy, G. Puppo, G. Russo, Central WENO schemes for hyperbolic systems of conservation laws, Math. Model. Numer. Anal. 33 (1999) 547–571.
[23] D. Levy, G. Puppo, G. Russo, Compact central WENO schemes for multidimensional conservation laws, SIAM J. Sci. Comput. 22 (2) (2000) 656–672.
[24] T. Linde, P.L. Roe, Robust Euler codes, in: 13th Computational Fluid Dynamics Conference, AIAA, 1997, Paper-97-2098.
[25] X. Liu, S. Osher, T. Chan, Weighted essentially non-oscillatory schemes, J. Comput. Phys. 115 (1994) 200–212.
[26] H. Luo, J.D. Baum, R. Lohner, A Hermite WENO-based limiter for discontinuous Galerkin method on unstructured grids, J. Comput. Phys. 225 (2007) 686–713.
[27] J. Qiu, C.-W. Shu, Hermite WENO schemes and their application as limiters for Runge-Kutta discontinuous Galerkin method: one dimensional case, J. Comput. Phys. 193 (2003) 115–135.
[28] J. Qiu, C.-W. Shu, Runge-Kutta discontinuous Galerkin method using WENO limiters, SIAM J. Sci. Comput. 26 (2005) 907–929.
[29] J. Qiu, C.-W. Shu, A comparison of troubled-cell indicators for Runge-Kutta discontinuous Galerkin methods using weighted essentially nonoscillatory limiters, SIAM J. Sci. Comput. 27 (2005) 995–1013.
[30] J. Qiu, C.-W. Shu, Hermite WENO schemes and their application as limiters for Runge-Kutta discontinuous Galerkin method II: two dimensional case, Comput. Fluids 34 (2005) 642–663.
[31] W.H. Reed, T.R. Hill, Triangular Mesh Methods for the Neutron Transport Equation, Tech. report LA-UR-73-479, Los Alamos Scientific Laboratory, Los Alamos, NM, 1973.
[32] C.-W. Shu, Essentially non-oscillatory and weighted essentially non-oscillatory schemes for hyperbolic conservation laws, in: B. Cockburn, C. Johnson, C.-W. Shu, E. Tadmor (Eds.), Advanced Numerical Approximation of Nonlinear Hyperbolic Equations, in: A. Quarteroni (Ed.), Lecture Notes in Mathematics, vol. 1697, Springer, 1998, pp. 325–432.
[33] C.-W. Shu, TVB uniformly high-order schemes for conservation laws, Math. Comput. 49 (1987) 105–121.
[34] C.-W. Shu, High order weighted essentially non-oscillatory schemes for convection dominated problems, SIAM Rev. 51 (2009) 82–126.
[35] C.-W. Shu, S. Osher, Efficient implementation of essentially non-oscillatory shock-capturing schemes, J. Comput. Phys. 77 (1988) 439–471.
[36] C.-W. Shu, S. Osher, Efficient implementation of essentially non-oscillatory shock capturing schemes II, J. Comput. Phys. 83 (1989) 32–78.
[37] G. Sod, A survey of several finite difference methods for systems of nonlinear hyperbolic conservation laws, J. Comput. Phys. 27 (1978) 1–31.
[38] P. Woodward, P. Colella, The numerical simulation of two-dimensional fluid flow with strong shocks, J. Comput. Phys. 54 (1984) 115–173.
[39] X. Zhong, C.-W. Shu, A simple weighted essentially nonoscillatory limiter for Runge-Kutta discontinuous Galerkin methods, J. Comput. Phys. 232 (2013) 397–415.
[40] J. Zhu, J. Qiu, A new fifth order finite difference WENO scheme for solving hyperbolic conservation laws, J. Comput. Phys. 318 (2016) 110–121.
[41] J. Zhu, J. Qiu, A new type of finite volume WENO schemes for hyperbolic conservation laws, J. Sci. Comput. 73 (2017) 1338–1359.
[42] J. Zhu, J. Qiu, C.-W. Shu, M. Dumbser, Runge-Kutta discontinuous Galerkin method using WENO limiters II: unstructured meshes, J. Comput. Phys. 227 (2008) 4330–4353.
[43] J. Zhu, C.-W. Shu, A new type of multi-resolution WENO schemes with increasingly higher order of accuracy, J. Comput. Phys. 375 (2018) 659–683.
[44] J. Zhu, C.-W. Shu, A new type of multi-resolution WENO schemes with increasingly higher order of accuracy on triangular meshes, J. Comput. Phys. 392 (2019) 19–33.
[45] J. Zhu, X. Zhong, C.-W. Shu, J. Qiu, Runge-Kutta discontinuous Galerkin method with a simple and compact Hermite WENO limiter, Commun. Comput. Phys. 19 (2016) 944–969.